



Virtual cochlear implantation for personalized rehabilitation of profound hearing loss^{☆☆☆}

Daniel Schurzig^{a,b,*}, Felix Repp^c, Max E. Timm^d, Cornelia Batsoulis^b, Thomas Lenarz^{a,d}, Andrej Kral^{a,d,e}

^a Institute of AudioNeuroTechnology & Department of Experimental Otolology, ENT Department, Hannover Medical School, Hannover, Germany

^b MED-EL Research Center, Hannover, Germany

^c Otofig GmbH, Hannover, Germany

^d Department of Otolaryngology, Hannover Medical School, Hannover, Germany

^e Department of Biomedical Sciences, Faculty of Medicine and Health Sciences, Macquarie University, Sydney, Australia

ARTICLE INFO

Article history:

Received 22 September 2022

Revised 9 December 2022

Accepted 26 December 2022

Available online 27 December 2022

Keywords:

Individualized cochlear implantation

Insertion angle prediction

Cochlear tonotopy

Outcome variability

Surgical planning

ABSTRACT

In cochlear implantation, current preoperative planning procedures allow for estimating how far a specific implant will reach into the inner ear of the patient, which is important to optimize hearing preservation and speech perception outcomes. Here we report on the development of a methodology that goes beyond current planning approaches: the proposed model does not only estimate specific outcome parameters but allows for entire, three-dimensional virtual implantations of patient-specific cochlear anatomies with different types of electrode arrays. The model was trained based on imaging datasets of 186 human cochleae, which contained 171 clinical computer tomographies (CTs) of actual cochlear implant patients as well as 15 high-resolution micro-CTs of cadaver cochleae to also reconstruct the refined intracochlear structures not visible in clinical imaging. The model was validated on an independent dataset of 141 preoperative and postoperative clinical CTs of cochlear implant recipients and outperformed all currently available planning approaches, not only in terms of accuracy but also regarding the amount of information that is available prior to the actual implantation.

© 2023 The Authors. Published by Elsevier B.V.

This is an open access article under the CC BY license (<http://creativecommons.org/licenses/by/4.0/>)

1. Introduction

Predicting the outcomes of surgical interventions, particularly those using medical implants, is of key importance for patient counselling but has been an elusive goal so far. The most successful neuroprosthetic device, the cochlear implant (CI), is a model system for such approaches. Since the outcomes of cochlear implantation are variable, the benefit of the intervention depends on the selection of the implant electrode with respect to the highly individual anatomical morphology of the receiving organ, the cochlea.

[☆] Conflict of Interest: DS, FR and CB are partly or fully employed by medical industry. The presented model is public domain and while the data have been at the first step collected for one brand of cochlear implants, it provides the possibility of extension to other implant brands. We do not see any conflict of interest in the present study.

^{☆☆} This is an original work that has not been published nor submitted to another journal.

* Corresponding author.

E-mail address: schurzig.daniel@mh-hannover.de (D. Schurzig).

A CI is the only option to compensate for severe to profound hearing loss, allowing for open-set speech understanding after implantation (Blamey et al., 2013; Carlson, 2020; Kral and O'Donoghue, 2010). It is achieved by direct neuroprosthetic stimulation of the auditory nerve through an electrode array which is surgically placed in the inner ear and bypasses the non-functional organ of Corti by electric fields (Clark, 2003). CIs have been provided to approximately 1 million subjects. While outcomes have been exceeding initial expectations, there are still ~25% of subjects who underperform. In 78% of these cases the underperformance has an unknown cause (Lazard et al., 2012; Moberly et al., 2016; Pisoni et al., 2017). While the variability remains largely unexplained in an individual subject, general influential factors are well-known. They include cochlear factors (like “cochlear health”, i.e. the preservation of auditory nerve fibers), central auditory factors, cognitive factors and device related factors (Kral et al., 2016).

Device-related factors are linked to the exact position of the implant in the cochlea, which varies between patients even with the same electrode due to the variability of the human cochlea in both size and shape (Hardy, 1938; Kawano et al., 1996; Erixon et al., 2009; Rask-Andersen et al., 2011; Koch et al., 2017a; Timm et al.,

2018; Avci et al., 2014). These variations influence the eventual intracochlear position of the CI (Avci et al., 2017). Furthermore, since there is a large portfolio of different CI electrodes on the market (Dhanasingh and Jolly, 2017), the exact intracochlear position of the implant varies depending on both the inserted electrode array and the individual cochlear morphology. This is highly relevant since the exact position of the CI array has a major impact for the outcomes, as exemplified on the achieved insertion depth (measured as “insertion angle (IA)” (Avallone et al., 2021; Schurzig et al., 2018a)):

1. Patients with functional residual hearing which can be preserved during CI surgery can benefit from the combined use of a hearing aid and a CI (Imsiecke et al., 2019a; Imsiecke et al., 2019b). Such hybrid approach - called electric-acoustic stimulation - substantially improves hearing outcomes (Buechner et al., 2017). Hearing preservation, however, negatively correlates with the IA of the electrode array (O’Connell et al., 2017; Lenarz et al., 2019). This is likely owed to the narrowing dimensions of the scala tympani (ST) in the second cochlear turn (Biedron et al., 2010; Schurzig et al., 2019; Wysocki, 1999; Rebscher et al., 2008). In addition, it could be shown that the height profile of the cochlea does not consistently increase (Avci et al., 2014). Instead, the cochlear spiral often shows substantial inconsistencies in its vertical incline, may dip down within the basal turn and show strong vertical increases/jumps rather than a consistent incline at the beginning of the second turn. The combination of this “rollercoaster” vertical profile (Avci et al., 2014) with the narrowing intracochlear spaces results in an increased contact between electrode array and intracochlear structures (Salcher et al., 2021), vibrational damping and an increased risk of implantation trauma. In combination with further, more localized intracochlear anatomical variations (Verbist et al., 2009; Avci, et al., 2014), contact pressures may be increased especially if the implanted array is not flexible enough to adjust to these variations.
2. Speech and pitch perception, on the other hand, improve with increasing IA and electrode length (O’Connell et al., 2017; Buechner et al., 2017; Roy et al., 2016). This interrelation is due to the location of the intracochlear neural structures (Helpard et al., 2020; Li et al., 2020) and the corresponding natural distribution of spiral ganglion neurons (Greenwood, 1990a; Stakhovskaya et al., 2007) stimulated by the implant: deeper insertions lead to a smaller mismatch between the natural tonotopic frequency distribution in the cochlea and the one imposed by the implanted array (Landsberger et al., 2015; Rader et al., 2016).

Consequently, there is a trade-off between risk of cochlear trauma and optimal cochlear coverage. Knowledge about the rollercoaster profiles and the presence/absence of steep vertical jumps at the transition between the first and the second cochlear turn, allow for quantification of the impact of deeper implantation on cochlear trauma. Given the large variability of cochlear size and microanatomy, only careful preoperative planning allows optimally balancing the risks and benefits in the individual subject using the individual electrode.

Modern clinical imaging techniques like cone beam computed tomography (CBCT) preclude the visualization of many anatomical details in the cochlea due to limited resolution (Schurzig et al., 2018a; Würfel et al., 2014; Timm et al., 2018; Meng et al., 2016). The missing, highly individual details in cochlear morphology can be, however, predicted by precise mathematical cochlear models (Pietsch et al., 2017; Pietsch et al., 2022; Schurzig et al., 2021a; Schurzig et al., 2021b; Margeta et al., 2022). Such models can be individualized based on parameters obtained from clinical imaging and include microanatomical information derived from high-

resolution laboratory methods applied postmortem, e.g., using micro computed tomography (μ CT) (Avci et al., 2014; Koch et al., 2017b; Schurzig et al., 2019; Margeta et al., 2022). The mathematical models thus allow overcoming the insufficient resolution of the clinical CT by predicting the details of the anatomy that are otherwise not discernible but can be predicted for the cochlea of the given overall size and proportions. However, current, validated mathematical models only predict the spiral shape of the lateral wall (LW) of the cochlea. A “virtual cochlear implantation” to assess the position of the potential implant in the individual patient before surgery requires a comprehensive, three-dimensional volumetric representation of the individual cochlear anatomy which is not available at this point. Such virtual implantation might enable the surgeon to select the most appropriate type of electrode array for a given cochlea, prepare for the implantation procedure and better predict its outcomes.

Based on a large dataset of 327 individual human cochleae, the current study provides such a validated 3D volumetric model that allows for virtual cochlear implantation. The study analyzed high resolution μ CT scans ($N = 15$) of human cadaver cochleae, as well as a training set ($N = 171$) of preoperative and postoperative clinical CBCT images of the cochleae before and after implantation. The resulting volumetric model allows for determining not only an individualized volumetric 3D shape of the individual patient-specific cochlea, but also for predicting the location of the entire electrode array trajectory inside this cochlea and the cochlear frequency representation of the electrode contact locations. The model was validated by comparing the planning and the actual outcomes of implantations on a large independent validation set of 141 cochleae. The study reveals a high precision of the 3D virtual implantation. The model can be tuned for different electrode arrays and be downloaded for free at https://neuroprostheses.com/AK/Virtual_Implantation.html.

2. Material and methods

The study consists of six steps of analysis: (i) we analyzed the microanatomy of the scalar shapes for the volumetric model on 15 μ CT images of human cochleae. We then normalized the resulting 1044 manually traced cross-sectional shapes and generated a mean 3D model of the scalar microanatomy. (ii) These results were numerically projected onto three existing approaches to determine the shape of the cochlear spiral from individual, clinical CBCTs. This provided three different 3D full volumetric models of the individual cochlea. (iii) In a training dataset of 171 cochleae implantation was performed, and the implant electrode trajectory was assessed using a second CBCT. A procedure was developed to combine the pre-implantation and post-implantation scans (optimized for the bony structure and the implant electrode, respectively). This allowed for determining the distance of the electrode from the LW along the cochlea from base to apex. These data were used for the next step, the virtual implantation. (iv) Two models of the implant location, one with constant displacement and one using the above 171 data, were combined with a 3D model of the corresponding cochlear implant electrodes. This allowed for the virtual implantation of each cochlea. (v) The surgeon used these results in an individualized approach to select the most appropriate implant array for the individual patient in the remaining 141 cochleae of a validation dataset. (vi) After implantation, the virtually-implanted cochleae were projected back onto the combined scans (before and after implantation) to compare the predicted and actual location of the electrode and validate the model. For this purpose, the electrode array (both predicted and postoperatively assessed) was reduced to a simple spiral of the geometric means at each location, and their difference quantified the prediction error. A detailed description of the individual analysis steps is given in the following.

2.1. Cochlear specimens

For the present study, 15 postmortem μ CT scans of unimplanted cochleae with normal anatomies were analyzed to extract information on the intracochlear microanatomy. Furthermore, CBCT images from 312 cochleae obtained from subjects undergoing cochlear implantation were used. All clinical CT images were anonymized. The institutional ethics committee at Hannover Medical School approved the use of anonymized imaging data obtained within the clinical routine. Each one of the 312 clinical datasets consists of preoperative and postoperative CBCT scans of the respective cochlear implant patient, implanted by a large group of 16 surgeons with either MED-EL FLEX20 ($N = 46$), FLEX24 ($N = 60$), FLEX26 ($N = 3$), FLEX28 ($N = 196$) or FLEXSOFT ($N = 7$) electrode arrays. Only patients with normal anatomies and without additional disorders like otosclerosis and meningitis were investigated within this study. Preoperative scans were acquired within a timeframe of 3 month prior to surgery, while postoperative scans were typically performed right before the suture was closed. The total number of 312 sets of preoperative and postoperative CBCT scans was divided into a training and a test dataset. The **training dataset** included 171 (FLEX20: $N = 31$; FLEX24: $N = 34$; FLEX26: $N = 1$; FLEX28: $N = 101$; FLEXSOFT: $N = 4$) and the **test dataset** included 141 (FLEX20: $N = 15$; FLEX24: $N = 26$; FLEX26: $N = 2$; FLEX28: $N = 95$; FLEXSOFT: $N = 3$) patients respectively. The training dataset was used to extract important parameters for the model, the validation dataset was used to validate the outcomes by comparing the prediction of the model with the true location of the array after implantation. The division was based on both the total number of patients as well as which patients had been part of previous studies (Schurzig et al., 2018a; Avallone et al., 2021) to allow for comparisons to former results. From the test dataset an extensive detailed analysis of the 3D shape was additionally performed on a subset of 19 subjects.

2.2. Assessment of variance in cross-sectional shapes

We first analyzed the shape of the cross-sectional microanatomy of the ST and scala vestibuli (SV), whereas scala media was added to the SV due to limited visibility of the Reissner's membrane. To have sufficient resolution, these measurements were performed using μ CT images. In brief, the 15 fresh frozen temporal bones from human body donors were placed in a SCANCO MicroCT 100 scanner (version 1.1, SCANCO Medical AG, Switzerland) and scanned at 70kVp and 114 or 88 μ A with AlO5 or CuO1 filtering, yielding a homogeneous voxel size of 10 μ m.

The scans were imported into a custom research software specifically designed for assessing the cochlear anatomy (Lexow et al., 2016), and the cross-sections of the scalae were segmented along the entire cochlear spiral for each one of the 15 cochleae (Timm et al., 2018). In order to generate average representations of the scalae, the centroid of each cross-section was computed and used to superimpose the individual cross-sections for each cochlear angle from 0° to 810° (which was the largest common angular length) in 1° steps. Prior to averaging the total of 1044 individual cross-sections of ST and SV respectively, differences in cross-sectional rotations were compensated by rotating the basilar membrane orientation to its cochlear angle specific average value (Schurzig et al., 2019), which was shown to preserve as many common cross-sectional features as possible (Schurzig et al., 2021a).

2.3. Assessment of individual cochlear anatomy with CI

As in our previous clinical investigations (for details, see (Schurzig et al., 2018a; Timm et al., 2018; Würfel et al., 2014)),

the assessment of the individual cochlear spiral geometry was performed using OsiriX MD. After loading the preoperative CBCT imaging, points were placed along the cochlear LW starting at the level of the center of the round window and proceeding to the apical end of the cochlea. The location of the CI array was assessed using the postoperative imaging data of the patient: the initial point was placed at the location at which the CI array enters the cochlea through the round window, followed by one point within the center of the artifact of each one of the intracochlear contacts. Since the segmentation points were placed centrally within the artifacts, it can be assumed that the trajectory defined by the coordinates of these points corresponds to the central axis of the CI array. The coordinates of both the LW and CI array tracing were then exported for further processing in Matlab (version R2018a, The MathWorks Inc., USA).

2.4. LW reconstruction

The individual segmentation points of the LW of each patient were loaded into Matlab to reconstruct the LW helix within the consensus cochlear coordinate system proposed in (Verbist et al., 2010), i.e. with the modiolus coinciding with the z axis and the center of the round window lying on the x axis. For an initial approximation of the corresponding transformation matrix T_{CT} from CT space to the consensus coordinate system, two points were employed to estimate the modular axis. The first one lay in the center of an auxiliary line connecting the first, most basal segmentation point P_1 with the one with the largest spatial distance to this point (P_4 in the example depicted in Fig. 1A), while the second point was the most apical LW segmentation point. The corresponding transformation matrix $T_{CT,init}$ was then calculated such that the central point of the auxiliary line coincides with the coordinate system's origin while the initial guess of the modiolus axis coincides with the z axis (Fig. 1B). In order to optimize the position of the LW segmentation within the consensus coordinate system, the radial distance of each segmentation point r_i to the z axis as well as the height of each point h_i relative to the xy plane were calculated. Based on these parameters, a residual function f_{res} was defined as

$$f_{res} = \sum_{i=2}^N (r_i - r_{i-1})^2 + \sum_{i=2}^{N-1} (h_i - h_{i-1})^2 \quad (\text{Eq. 1})$$

where N represents the total number of segmentation points, r is the radius and h the height of the individual points. The residual function f_{res} includes 2 least squares terms, one for the radii and one for the heights of the segmentation points. The function was composed such that its value becomes smaller when the changes in radii and height along the cochlear spiral become more consistent, i.e., for a gradually increasing radius and a gradually increasing height. Matlab's nonlinear programming solver *fminsearch* was then used in combination with the initial guess $T_{CT,init}$ to minimize the residual function and hence derive the desired transformation matrix $T_{CT,min}$ which yields the optimized position of the LW points within the consensus coordinate system. Fig. 1C shows the radial and height profiles of one LW spiral before and after the minimization, and the corresponding LW spiral with the optimized modiolus is depicted in Fig. 1D. After repositioning, each individual LW helix was computed by interpolating the radius $r(\varphi)$ and height $h(\varphi)$ of the corresponding segmentation points (Fig. 1D). This type of reconstruction will be referred to as LW tracing in the following. Note that all individual transformation matrices $T_{CT,min}$ were saved to allow for the projection of the reconstructed anatomy and predicted CI array location back into the CT space, enabling visualization of the corresponding virtual implantation within the imaging data.

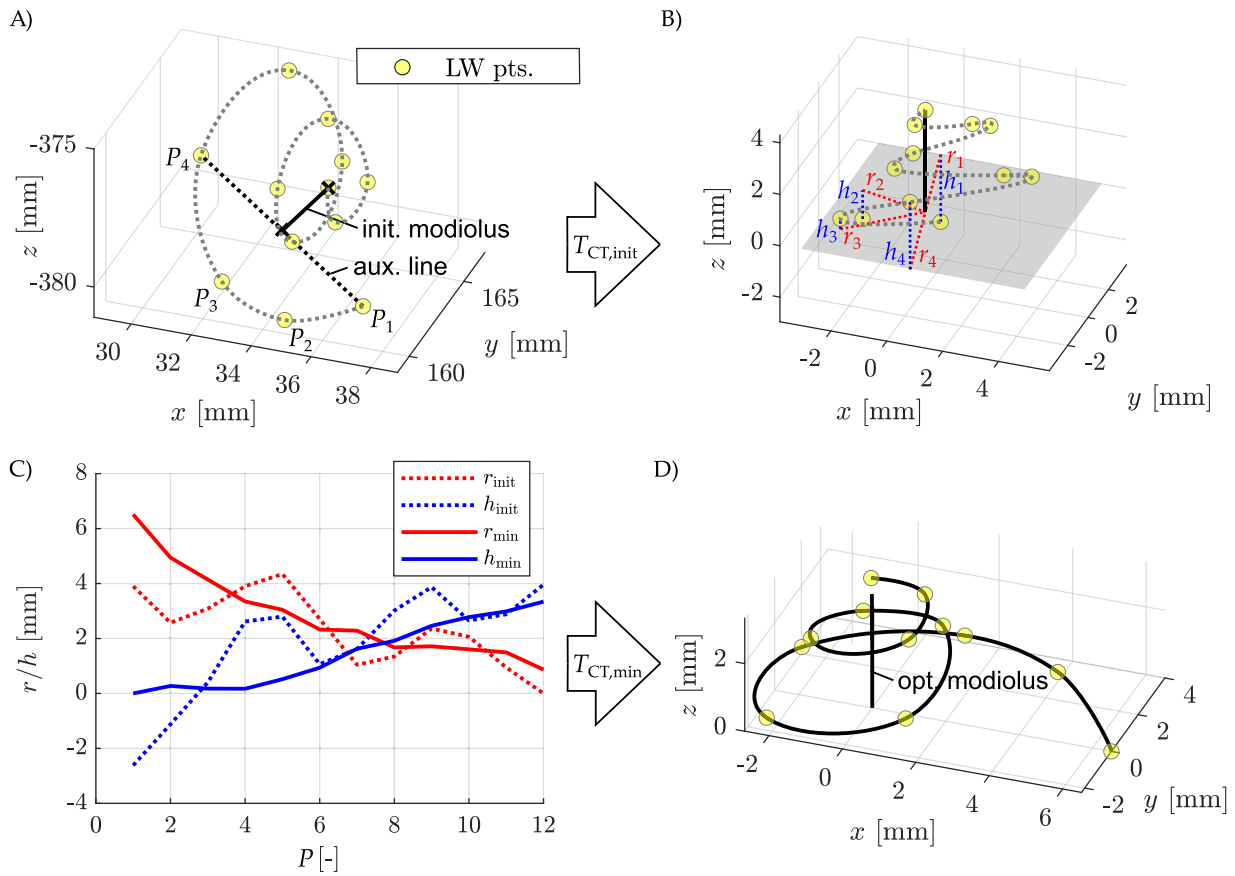


Fig. 1. A) LW segmentation points in CT space with LW spiral shape indicated by the dashed line. The initial guess of the modiolus axis was used to define an initial guess $T_{CT,init}$ of the transformation into the consensus coordinate system and derive (B) the radii and height values of all segmentation points. C) Minimization within Matlab yielded the final transformation matrix $T_{CT,min}$ resulting in smoothly changing radial and height profiles of the LW points from base to apex. D) Optimized, reconstructed LW profile in the standardized coordinate system.

Since the described assessment of the LW in OsiriX MD is time consuming and hence difficult to integrate into the clinical routine, two alternative approaches were employed to reconstruct the LW. The elliptic-circular approximation (ECA) method (Schurzig et al., 2018b) was shown to yield very accurate approximations of the length of the LW and corresponding IAs (Mertens et al., 2020; Avallone et al., 2021) and exclusively dependent on the individual cochlear diameter A and width B (Escudé et al., 2006; Erixon and Rask-Andersen, 2013; Schurzig et al., 2018c; Anschuetz et al., 2018). In order to yield a three-dimensional representation of the LW, the model was integrated into this study in a slightly different manner as the one proposed by the authors: first, the individual LW basal turn length $BTL_{LW,ind}$ was computed according to

$$BTL_{LW,ind} = 1.18A + 2.69B - \sqrt{0.72 AB} \quad (\text{Eq. 2})$$

Note that in this study, the individual values of A and B were extracted from the above LW tracing to exclude the influence of assessment errors onto model performance differences. In the original study, the authors then proposed to use so-called p_{BTL} values to compute the length of the cochlea at specific locations. Within the present study, the coordinates of the same mean spiral which lead to these p_{BTL} values were scaled such that the BTL of the mean LW spiral $BTL_{LW,mean}$ matched the above approximation:

$$[x, y, z]_{LW,ind}^T = BTL_{LW,ind}/BTL_{LW,mean} \cdot [x, y, z]_{LW,mean}^T \quad (\text{Eq. 3})$$

Hence, this approach is basically the numerical version of the original ECA method.

The second LW model integrated into this study is the recently proposed regression scaling (RS) model (Schurzig et al., 2021a).

This model was shown to not only mimic the overall cochlear anatomy very well, but also to be capable of reconstructing localized height variations (local dips and jumps) of the cochlear spiral. Its key elements are the two matrices \hat{M}_r and \hat{M}_h which comprehend various regression parameters derived in an analysis of 108 corrosion casts of human cochleae. These matrices basically allow for the extrapolation of the individual cochlear radius and height from 360° in 90° steps up to the apex based on the assessment of the basal cochlear radii at $0^\circ, 90^\circ, 180^\circ$ and 270° . The whole set of radii and height values can then be used for a section-wise morphing of a mean model. Within the present study, the radii from 0° to 270° were computed based on the corresponding values of A and B and the mean ratios of the radii r_0 to r_{180} and r_{90} to r_{270} respectively:

$$r_0 = 0.647 \cdot A \quad (\text{Eq. 4})$$

$$r_{90} = 0.581 \cdot B \quad (\text{Eq. 5})$$

$$r_{180} = 0.353 \cdot A \quad (\text{Eq. 6})$$

$$r_{270} = 0.419 \cdot B \quad (\text{Eq. 7})$$

The overall radii and height information of the individual spirals could then be computed as proposed in (Schurzig, et al., 2021a):

$$[r_{360}, r_{450}, r_{540}, \dots]^T_{Ct,a} = \hat{M}_r \cdot [1, r_0, r_{90}, r_{180}, r_{270}]^T_{Ct} \quad (\text{Eq. 8})$$

$$[h_0, h_{90}, h_{180}, \dots]^T_{Ct,a} = \hat{M}_h \cdot [1, r_0, r_{90}, r_{180}, r_{270}]^T_{Ct} \quad (\text{Eq. 9})$$

A detailed description on the subsequent section-wise scaling procedure can be found within the original publication as well.

2.5. Cochlear model generation

In order to enhance the LW models described above to full volumetric representations of the individual cochleae, the average anatomies of the ST and SV (Section 2.2) were used. These cross-sections and a point representing the LW contour at the respective locations were made available from the center of the round window to the beginning of the helicotrema in 1° steps, resulting in a total of 811 cross-sections from 0° to 810° . To provide the possibility of combining this information with the individualized shape of the given cochlea, the apical to basal positional information was normalized using the cochlear angle, which simplified the assembly of the volumetric model in comparison to employing the normalized metric length as proposed by Greenwood (Greenwood, 1990a).

The LW contour was obtained from the tracing of the individual cochlea. Additionally, the two most precise cochlear models were used to generate an alternative LW contour using A, B and their transection by the modiolus, as well as cochlear height from the clinical CT as the input. The cross-sections were then combined with the respective locations along the three resulting spirals yielding a 3D volumetric cochlea representation.

2.6. Electrode array location prediction

Since the LW can typically be distinguished within clinical CBCT data, the location of an electrode array inside the cochlea is typically described relative to the LW. Alexiades et al. (Alexiades et al., 2015) approximated that on average, straight electrode arrays lie 0.35 mm away from the LW. Within the current study, the geometrical data of the 171 patients in the training dataset was analyzed according to the approach proposed by Salcher et al. (Salcher et al., 2021) to generate electrode array and IA dependent average relations of the distance between the central path of the electrode array and the LW. For all 171 patients, the LW and CI electrode were traced within the preoperative and postoperative imaging, respectively. Tracing the LW in preoperative imaging was chosen because the LW contour is often blurred by the contact artifacts of the inserted electrode array in postoperative CT scans. In order to assess the location of the CI array relative to the LW, each CI tracing was then registered onto the corresponding LW spiral using the helix-based registration method (*HelReg*) proposed in (Schurzig et al., 2018a). This method was chosen because it was shown to be well-suited for accurately assessing postoperative IAs and coverage values while being computationally much faster than image-based registrations. After registration, the insertion depth, IA and radial distance of each contact to the LW was computed for each one of the 171 patients, yielding a total of 2052 insertion depth, IA and distance values. The final distance profiles for predicting the CI array locations of the validation dataset were then derived by grouping these values according to the different types of electrode arrays and performing a moving average computation of the radial distance values relative to the IA. Note that here again all surgeons active at the Otolaryngology clinics were involved, thus the mean results are not specific to one surgeon. Furthermore, results from 5 different electrode arrays were pooled together, as described above. These results thus represent a mean from all electrodes (that were, however, all LW electrodes).

Both the consistent offset of 0.35 mm and the ones calculated according to Salcher et al. (Salcher et al., 2021) were then employed to approximate the path of the different electrode arrays as follows:

Once the model of an individual cochlea was generated according to the description above, in order to obtain the location of the cochlear implant, the profile of the LW as described by the current model was projected radially toward the modiolus. The projection (the displacement) was either constant 0.35 mm or varied according to the LW distance profile $d_{LW}(IA)$ of the array to be inserted. As mentioned above, these electrode-specific distance profiles were determined based on geometrical evaluations of the 171 sets of preoperative and postoperative clinical imaging of the training dataset. In a second step, this projection was translated vertically such that it lies in the center of the ST at that radial location. The employment of geometrical information of the electrode array to be inserted then allowed for the creation of a 3-dimensional, volumetric representation of the electrode array inside the cochlea with an insertion depth according to the postoperatively assessed value. Deviations of predicted and true values hence originate from the virtual implantation algorithm alone and are not affected by incomplete insertions or ones beyond the marker point (see e.g. (Avallone et al., 2021) for more details). This procedure was chosen in order to evaluate the accuracy of the algorithm alone. Considering the three different cochlear models and two different LW distance assumptions, this yields 6 predictions for each one of the 141 cochleae of the validation dataset and 846 predictions in total. All predictions were compared to the postoperatively assessed trajectories of the individual arrays to evaluate the accuracy of predicted IAs.

For a subset of 19 patients of the validation dataset, registration from postoperative to preoperative imaging was additionally performed using an image-based registration method (Schurzig et al., 2018a). This type of registration is more elaborate and time consuming than the helix-based type but allows for reliable spatial evaluations of predicted and postoperatively assessed array location. Hence, this subset was used to evaluate the radial and height differences of predicted and postoperatively assessed array location.

Finally, visualization of virtual CI insertions inside the corresponding imaging data was achieved by transforming the corresponding models of cochlea and electrode array back into the imaging coordinate system and then exporting these models in stl format, which can be imported into most commercially and freely available DICOM viewers.

2.7. Error evaluation

Two types of validation have been performed for the present model. One was based on the dataset of 141 implantations and involved a simplified comparison of the implanted electrode with the LW spiral. The other one was based on comparison of the complete 3D dataset of the model with the 3D imaging dataset. This latter comparison involved a smaller number of subjects ($N = 19$) but required a more extensive alignment of 3D datasets. Here, all surgeons active at MHH were involved in implantations, and 6 electrode types, as mentioned above.

1. The CI array tracings of the 141 patients within the test dataset were registered to the corresponding tracings of the LW spirals using the *HelReg* method described in (Schurzig et al., 2018a). As a result, both the postoperatively assessed reference and the predicted CI array paths were available for each one of the 141 reconstructed cochleae. This registration result was then employed to calculate the deviations between predicted and postoperatively assessed reference IAs for each one of the inserted electrode contacts. This method does not involve the whole anatomical dataset, rather it compares the 3D shape of the implanted electrode to the LW spiral.

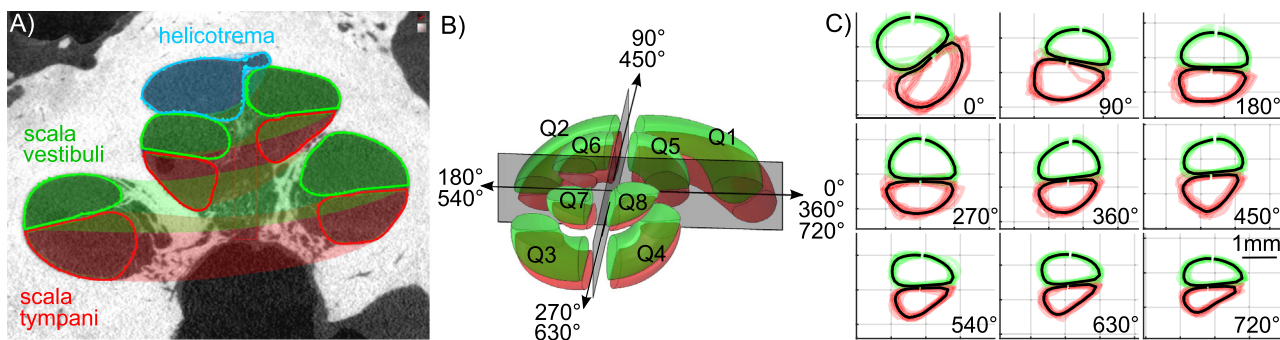


Fig. 2. A) Tracing of the scalar spaces in one example μ CT dataset, shown at the mid-modiolar section; red color corresponds to ST, green color to the SV, helicotrema is marked in blue. B) 3D representation of the average human cochlea (red: ST; green: SV) divided quadrants Q. C) Individual and mean cross-sectional shapes of the cochlear quadrants Q1-Q8 (apical turn not shown, the very last quadrant covers the helicotrema where the scalae unite).

2. In addition, we also wanted to know details about the spatial deviation between predicted and reference trajectory of the CI array. For this, a comparison of the complete 3D model with the imaging dataset had to be performed, with the particular difficulty of 3D alignment of the model with the DICOM dataset of the imaging. That is why we randomly picked 5 patients of each electrode group for which we also performed an image-based registration in 3D Slicer (Fedorov et al., 2012) as described in (Schurzig et al., 2018a). Note that the FLEX26 and FLEXSOFT were excluded from this investigation due to the small number of patients. For the 5 selected patients of each one of the other groups, accurate spatial descriptions of the electrode locations were available and could be compared to the predicted ones to calculate radial and height deviation of predicted and reference trajectory.

2.8. Statistics

All statistical evaluations were conducted in Python (version 3.7, Python Software Foundation, USA) using the Scipy library (version 1.2.1). Direct comparisons were performed using two-sided Mann-Whitney-Wilcoxon tests and two-way ANOVAs, with post-hoc comparisons using Fisher's least significant difference procedure, all at 5% significance level.

3. Results

Firstly, with a homogeneous voxel size of 10 μ m, 15 cochlear μ CT datasets allowed for the tracing of the microanatomy of the scalar spaces (Fig. 2A) at high resolution in steps of 22.5° from base to apex, resulting in a total of 1044 cross-sectional shapes. The derived cross-sectional profiles of the scalar spaces of the cochlear quadrants Q (Fig. 2B,C, cf. (Erixon et al., 2009)) revealed a good reproducibility of the shapes and a tendency for higher variability in the base of the cochlea (compared to the apex) and in ST (compared to SV). The cross-sectional profiles normalized in location to the basal-apical distance (as previously used in calculation of Greenwood function (Stakhovskaya et al., 2007)) allowed for the calculation of the mean cross-sectional profiles. This way we could assign a cross-sectional mean profile to a particular normalized angular distance from base to apex.

Adaptation of this volumetric model to 171 individual anatomies derived from clinical CT imaging (training dataset) was established using patient-specific LW spirals, which were computed using three different approaches: (i) clinical CTs were used to trace the LW by placing points along the spiral from base to apex, as previously documented (Timm et al., 2018;

Würfel et al., 2014) (Fig. 3A-B). The LW points were then interpolated into a 3D spiral in all 171 cochleae (Fig. 3C). In what follows we call this approach *LW tracing method*. Alternatively, detailed 3D models of the individual human cochlea were derived by measuring the two perpendicular axes of the cochlear base (A and B, Fig. 3A) as well as the spiral height H_s (Fig. 3B) in the same clinical CBCT images of the individual cochleae before implantation. These parameters have been used to individualize the previously validated mathematical cochlear models (Schurzig et al., 2018a, 2021a) yielding the LW spiral of the cochlea (Fig. 3D). They provide an excellent estimation of the overall cochlear duct length with deviations of less than 1 mm from the true cochlea as demonstrated by the leave one out approach from 108 corrosion casts. We compared two such models (Fig. 3D), namely (ii) the recently developed *RS model* (Schurzig et al., 2021a) and (iii) the *ECA model* (Schurzig et al., 2018a) which has been incorporated into the clinical software OTOPLAN® (CAScination AG, Switzerland) (Canfarotta et al., 2019; Mertens et al., 2020).

Subsequently, each spiral shape of the LW (Fig. 3C and D) and the mean profiles of the scalar spaces (Fig. 3E) were combined to the volumetric 3D computational model of the individual cochleae (Fig. 3F). Such model substantially extends previous LW models by incorporating the full 3D dataset at microscopic resolution, allowing to study the presumed individual cochlea in the computer at high resolution.

The cochlear implant was subsequently virtually "implanted" into such individualized cochlea. In addition to a 3D model of the implant electrode, this approach used the LW spiral to approximate the 3D course within the individual cochlea (Fig. 3F). It was displaced in the modiolar direction either by assuming a constant distance from modiolus of 0.35 mm (Alexiades et al., 2015), due to the anatomy essentially corresponding to a situation when the electrode corpus leans on the LW, or by using displacement data that were derived in the present study from CBCT scans of implanted cochleae ($N = 171$, see Fig. 4A). To allow for pooling the data from different subjects, the intracochlear location had to be numerically averaged for each normalized angular cochlear location. This normalized location was used by exploiting standard methods (as used in the Greenwood mapping of frequency representation to cochlear position (Greenwood, 1990; Stakhovskaya et al., 2007)), validated in previous studies (Salcher et al., 2021). The use of the distances from the implanted cochlea had the standout advantage of allowing for the implant to follow the course determined by the mechanics of the electrode, as observed clinically. Particularly in the first 180° the electrode is not located at a constant displacement from the LW, but rather follows its own predetermined shape. This generates the first peak in the displacement data near 90° with peak values of above 1 mm distance (Fig. 4A). In the vertical direction the electrode was virtually positioned in

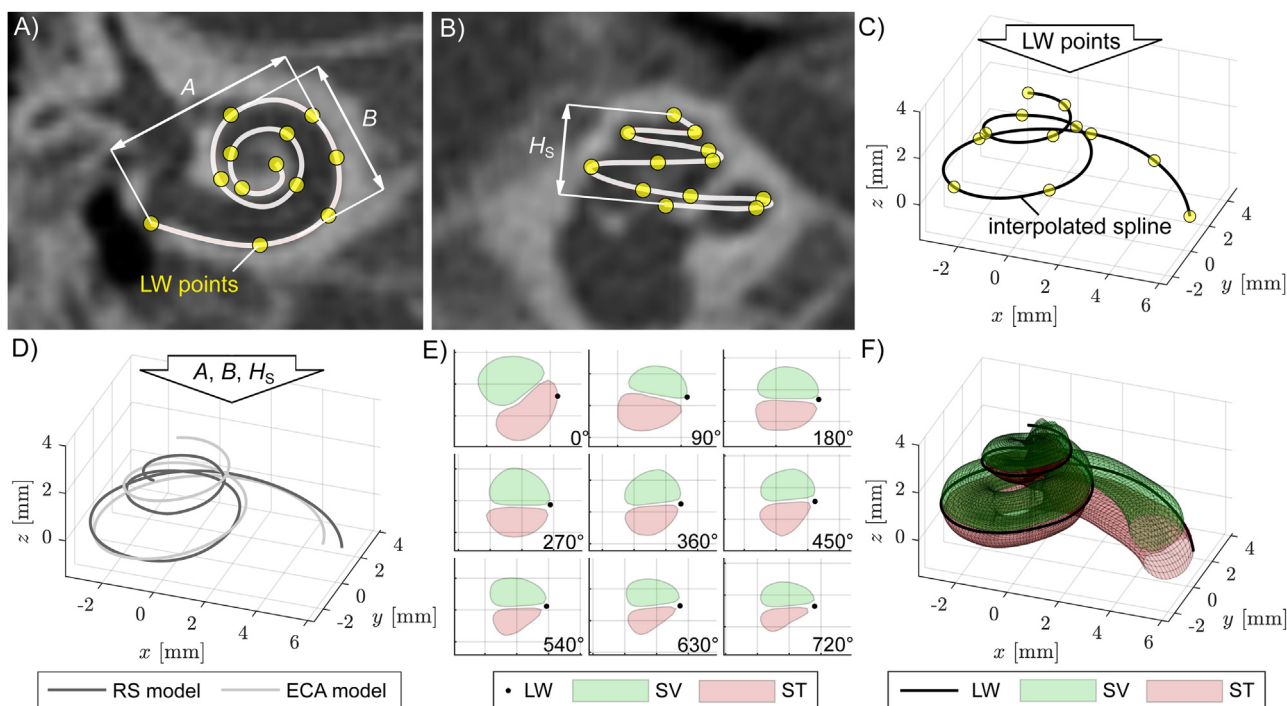


Fig. 3. A-B) Assessment of the patient specific anatomy in clinical imaging data either by placing points along the LW or by measuring the diameters of the cochlear base A and B and the spiral height H_s . C) Reconstruction of the traced LW by repositioning the LW points into the consensus cochlear coordinate system and interpolating the spiral shape. D) Reconstructions of the individual LW shape using two numerical models with the patient specific input values A, B and H_s . E) Cross-sections of ST and SV extracted from the average cochlear model presented in (Schurzig et al., 2021a). F) Full 3D geometrical representation of the cochlea based on a LW spiral combined with the average cross-sections.

the middle of the ST (Fig. 4C). The shape of the electrode array was modelled using a 3D skeleton of the implant array (Fig. 4D). This approach enabled us to predict the position of the electrode in the 3D cochlear model after successful cochlear implantation for the first time using analytical methods.

The virtual model was projected back into the CT image allowing for detailed visualizations of cochlear spaces and electrode array within preoperative clinical imaging (Fig. 5A-C). This procedure required a standardized orientation of the original scan, which was assured by use of the Verbist consensus coordinate system (Verbist et al., 2010). In addition, the model 3D result was projected into postoperative imaging in order to visually compare predicted and postoperatively assessed array locations and identify deviations from expected array trajectories (Fig. 5D-E).

Such numerical fusion of the model results with the imaging data was a precondition for validating the outcomes of the model based on an independent validation dataset of clinical data of 141 cochlear implant patients by comparing the individual predictions with the result of cochlear implantation. Each subject was implanted with the electrode selected based on preoperative analysis (virtual implantation) using one of the 5 electrode arrays. After the surgery, the location of the selected CI array in the cochlea was visualized in a second CT scan. Using the postoperative scan optimized for the metal electrode and the preoperative scan optimized for the bony tissue both images could be combined. This was achieved by registration of postoperative onto preoperative imaging data using a helix-based registration method (Schurzig et al., 2018a). Only such a fused image allowed analysing the exact location of the implant relative to the cochlear structures and quantifying its deviation from the predicted position. This approach enabled us to validate the developed model by quantifying the deviation of prediction and outcome in metric, angular and psychophysical measures. A Matlab based program which includes the anatomical model, the option to predict individual electrode ar-

ray predictions and a “stl export” function for further processing can be downloaded for free at https://neuroprostheses.com/AK/Virtual_Implantation.html.

For exact quantification in a second step, we reduced the electrode shape by generating a path along the centers of gravity of the electrode at each electrode contact, both in the model and in the real scans. This allowed us to subsequently quantify the difference between prediction and the actual outcome (Fig. 6). In the presented individual case, a difference in radial location is more obvious between 180 and 360° (Fig. 6B and C), whereas in the rest of the trajectories the data matched well. In the basal turn there is a notable difference in the vertical profile (Fig. 6D), which is likely owed to the way different surgeons guide the electrode into the cochlea as well as the large anatomical variability within the hook region of the cochlea (Li et al., 2007). The remaining vertical trajectory is then likely defined by the shape of the cochlea, and here the trajectories match well.

To quantify the overall performance of the model, we first analyzed the predicted IAs and corresponding place frequencies of the spiral ganglion cells inside the cochlea, which were derived according to the Greenwood function based on the model from (Helpard et al., 2021). These parameters are of key relevance for the outcome of cochlear implantation since these define the coverage of the neural receptors for electric inner ear stimulation. Altogether we analysed 141 implantations of different LW electrodes (see methods). Deviations of predictions to postoperatively assessed IAs and tonotopic frequencies (in semitones) are depicted in Fig. 7 for the different models and LW distance assumptions, pooled for the different electrode types and contacts. A two-way ANOVA revealed no interaction between the three models and LW distance assumption ($F(2,1331) = 1.86, p = 0.157$). Main effect analysis revealed a statistically significant effect of the LW distance assumption ($p < 0.001$) and no significant effect of model used ($p = 0.554$). A post-hoc comparison (Fisher’s

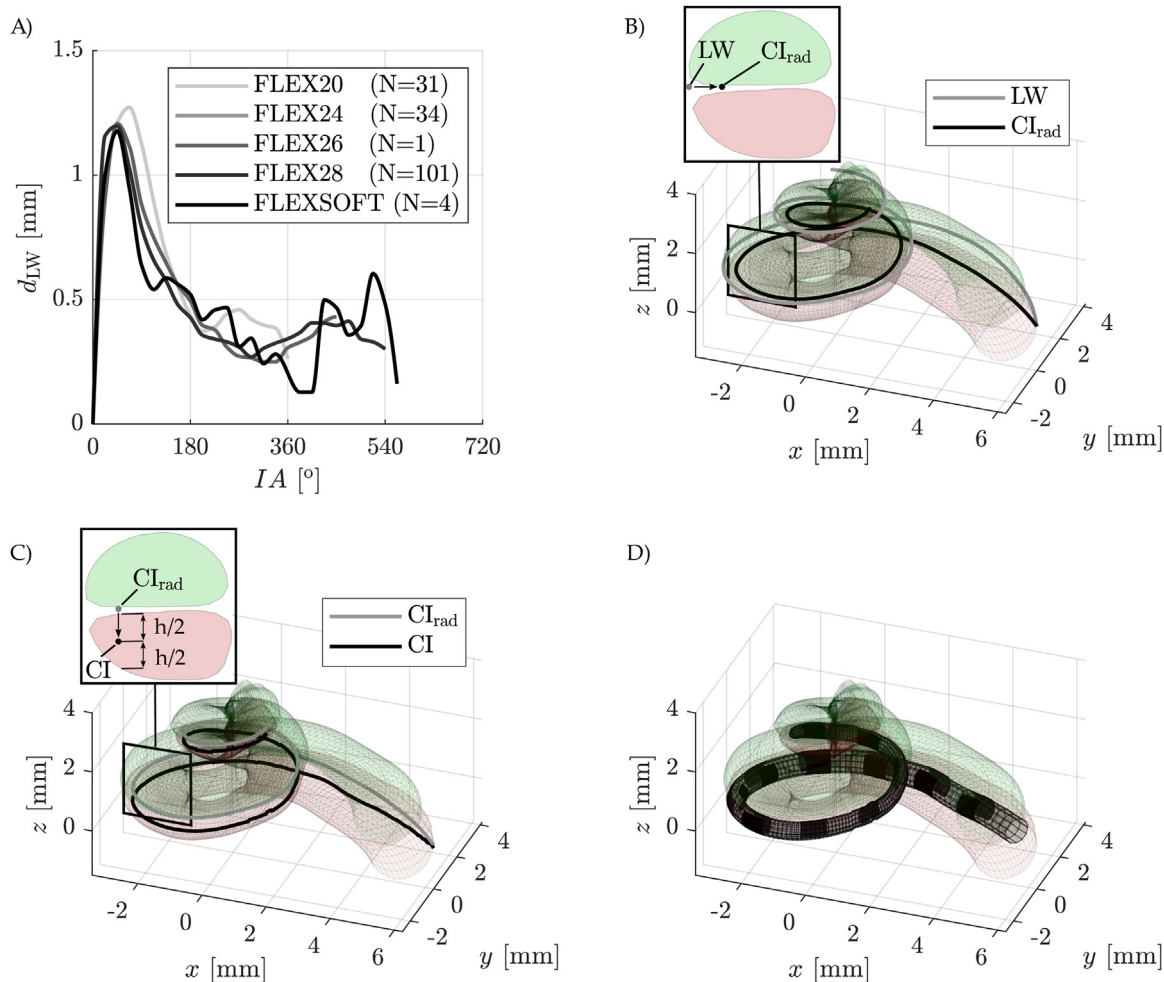


Fig. 4. A) Averaged radial distance values d_{LW} between the center of the array and the LW based on 171 patient datasets. Standard deviations not shown to improve clarity. B) Step 1 of generating the predicted electrode array path inside the cochlea is the radial projection of the most lateral point toward the modiolus either by a consistent offset of 0.35 mm or according to the electrode array and insertion angle specific value shown in A. C) the second step is a downward projection of this point to the vertically-centered location inside the ST. D) Geometrical data of the electrode array then allows a full 3D reconstruction of the array inside the cochlea.

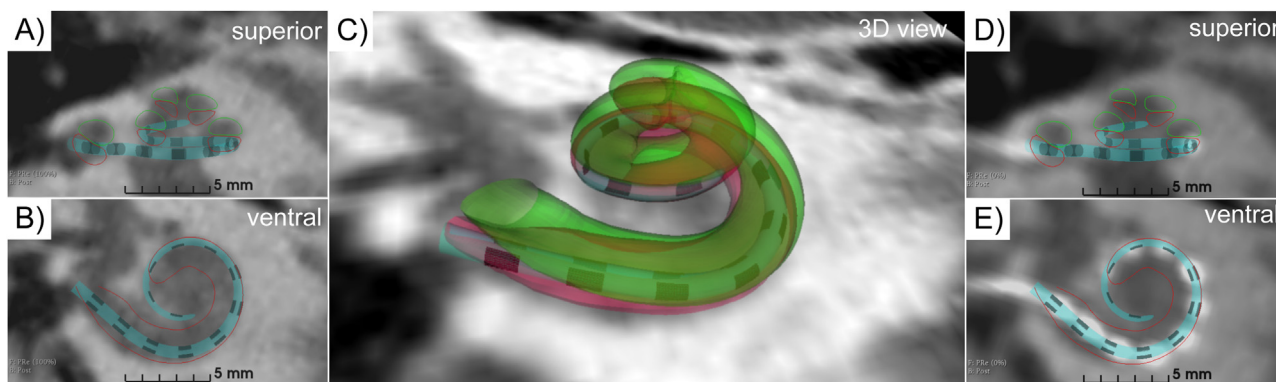


Fig. 5. Virtual cochlear implantation in the given individual temporal bone of the subject. A-C) depiction of cochlear anatomy and a predicted array location within preoperative imaging data. D-E) Comparison of predicted and postoperatively assessed array location.

least significant difference procedure) showed a significant reduction of prediction errors for all 3 models for the variable LW distance assumption (denoted as Salcher; tracing: $p = 4.29 \times 10^{-20}$; RS: $p = 1.57 \times 10^{-38}$; ECA: $p = 1.28 \times 10^{-46}$). The range of the errors were $< 45^\circ$, with 50% of the population within 20° medians of -5° , -3° and -2° and median absolute deviations of 13° , 12° and 13° for the tracing, RS and ECA models respectively. Approximation of the frequency allocation revealed that

the majority of the population shows errors within a range of 3 semitones (acoustically less than $\frac{1}{4}$ of an octave) with medians of 0.6, 0.4 and 0.2 semitones and median absolute deviations of 1.5, 1.5 and 1.7 semitones respectively. This demonstrates the astonishing precision of the prediction, suggesting that the virtual implantation approach presented here allows predicting the psychophysical consequences of the stimulation with the implant.

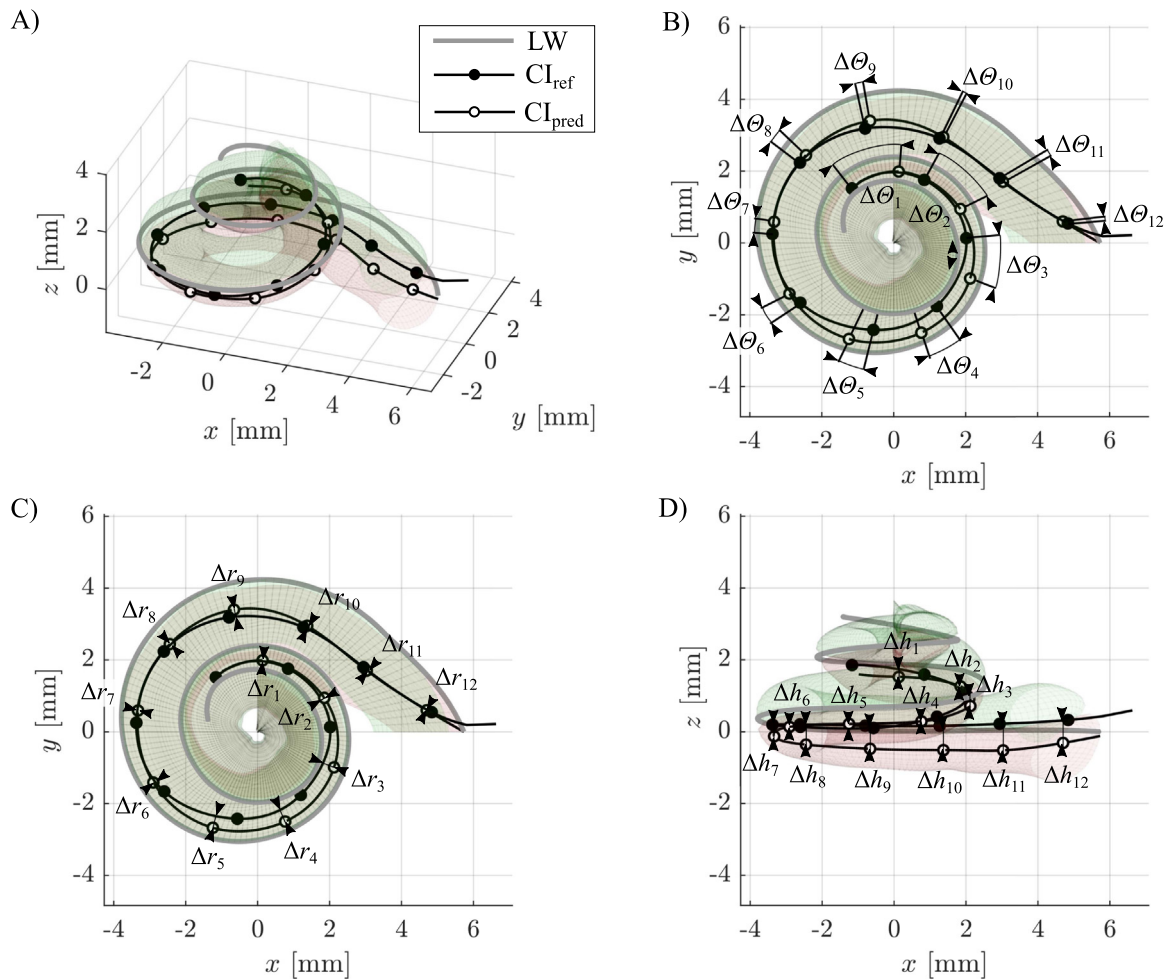


Fig. 6. A) After registration, both the postoperatively assessed reference trajectory of the inserted CI array as well as the predicted one are available to allow for the evaluation of deviations in (B) insertion angle, (C) radius and (D) height. One individual case shown. The trajectory is indicated by the solid line, the points represent the contact locations.

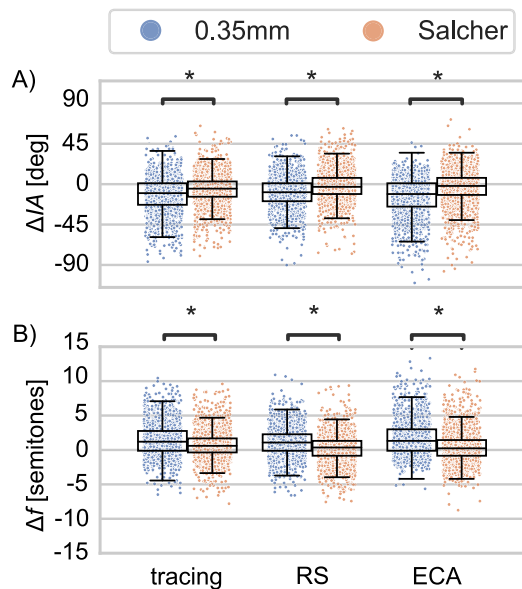


Fig. 7. Comparison of angular deviations between predicted and reference insertion angles pooled for all electrode types and contacts. Significant differences between the LW distance assumptions (consistent 0.35 mm vs. variable distances calculated according to Salcher et al.) were found for all models (141 subjects, for details see text).

Detailed, electrode and contact specific evaluations of prediction errors are provided in Figs. S1 and S2 and Tables S1 and S2 of the supplementary material for IAs and corresponding spiral ganglion frequencies respectively. These results indicate that the RS model yield the lowest prediction errors, which becomes particularly noticeable in the apex (i.e., for low contact numbers).

Finally, the spatial accuracy of the different model predictions was evaluated for a subgroup of the 141 cases of the validation dataset. 5 patients were randomly selected for the FLEX20, FLEX24 and FLEX28 groups for a contact-by-contact wise validation analysis of the results. Only 2 and 3 patients could be included for the FLEX26 and FLEXSOFT groups. The reference electrode locations for these evaluations were the postoperatively traced paths of the inserted arrays, which were registered to the preoperative imaging data using image-based registration (Schurzig et al., 2018a). One patient of the FLEXSOFT group had to be excluded from the investigation because the image-based registration did not converge, which resulted in a total number of 19 cases for this part of the investigation. The results of the spatial prediction accuracy are shown in Fig. 8.

A two-way ANOVA revealed for the radial deviation no interaction between the three models and LW distance assumption ($F(2,1367) = 0.18, p = 0.997$). Main effect analysis revealed a statistically significant effect of the LW distance assumption ($p < 0.001$) and a significant effect of model used ($p = 0.012$). Again, the Salcher approach decreased the prediction errors significantly

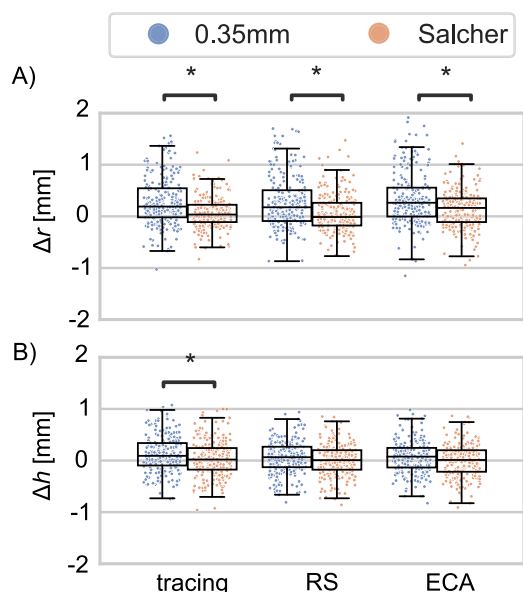


Fig. 8. Comparison of spatial deviations (A: radial deviations; B: height deviations) between predicted and postoperatively assessed electrode array trajectory pooled for all electrode types and contacts. Significant differences between the LW distance assumptions (consistent 0.35 mm vs. variable distances calculated according to Salcher et al.) were found for all models (19 subjects, for details see text).

(tracing: $p = 1.09 \times 10^{-6}$; RS: $p = 4.77 \times 10^{-5}$; ECA: $p = 1.40 \times 10^{-4}$). In model comparisons, the most recent RS model showed nominally smaller prediction errors than the other models, however, posthoc comparisons did not reach the level of significance. More detailed information on the contact specific, radial improvements and the statistical results are given in Fig. S3 and Table S3 of the supplementary material respectively.

For the heights errors, a two-way ANOVA revealed no interaction between the three models and LW distance assumption ($F(2,1367)=0.18$, $p = 0.833$). Main effect analysis revealed a statistically significant effect of the LW distance assumption ($p < 0.001$) and no significant effect of model used ($p = 0.07$). The variable LW distance approach denoted Salcher again lead to lower height errors for all 3 models, although this improvement only reached statistical significance for the tracing method ($p = 0.044$).

Also, in this more detailed analysis the precision of the prediction was high: for 50% of the population, it was within a range of 500 μm . Median errors with the Salcher method were 0.04 mm, -0.01 mm and 0.02 mm in radial and 0.02 mm, 0.01 mm and 0.01 mm in vertical direction for the tracing, RS and ECA models respectively. Median absolute deviations lay at 0.23 mm, 0.28 mm and 0.29 mm in radial and 0.27 mm, 0.24 mm and 0.24 mm in vertical direction for the tracing, RS and ECA models respectively. Fig. S3 of the supplementary material highlights that the improvements in the prediction using the Salcher model were achieved mainly in the base of the cochlea. Detailed information on the result of the ANOVA is given in Table S4 of the supplementary material.

The fact that posthoc comparisons did not reveal significant differences for radial or height deviations for the 3 models and the variable LW distance assumption shows that the incorporation of electrode specific insertion trajectories yields minimal spatial errors for all models.

4. Discussion

Based on a large dataset of 327 CI subjects, this study developed the first virtual cochlear implantation concept and validated

it using an independent validation set of implanted cochleae. The results show an exceptional precision in the prediction of the electrode location in the individual cochlea. Such virtual implantation provides a new tool for the selection of the best-fitting electrode for the individual subject's needs, with deviations between the same virtually and physically implanted cochlea that are within a range which will not influence outcome prediction, neither in anatomical aspects (as measured in mm) nor in psychophysical aspects (as measured in semitones). The model is free for download and use.

The high prediction accuracy is particularly astonishing as implantations of 16 different surgeons were used to validate the approach. While this introduces variability in the surgical approach despite the unified concept in our clinics, it closely mimics the everyday clinical situation. Despite this large number of surgeons, the algorithm was shown capable of predicting the electrode location with high accuracy. This could potentially be a consequence of the circumstance that for the investigated electrode arrays, the trajectory of the array inside the cochlea is determined more by the cochlear anatomy itself than the surgical approach.

The tracing of the electrode array in postoperative imaging involved points placed within the centers of the electrode contact artifacts, which were assumed to lie on the central axis of the electrode array. This is in agreement with several other studies in which this technique was applied (Avallone et al., 2021; Timm et al., 2018; Schurzig et al., 2018a). However, the apical 5 electrode contacts of all investigated MED-EL FLEX electrode arrays are single-sided. This could lead to artifacts which are located more closely to the electrode side on which these contacts are placed. In that case, the reconstructed CI electrode arrays could be inaccurate in radial and/or vertical direction by approximately 100–200 μm at the apical 5 contacts. The present results are all affected to a similar extent by this potential offset; therefore, the mutual comparisons are not influenced.

Preoperative planning tools like the proposed virtual implantation approach do not take all surgical aspects into account. A limited view onto the round window may, for instance, result in an incomplete electrode insertion or one beyond the marker point. That is why within our validation step, we used the postoperatively assessed insertion depth as an input parameter. Avallone et al. demonstrated how deviations between planned and surgically accomplished electrode insertion depths can lead to prediction errors (Avallone et al., 2021). Furthermore, the electrode array should also be sufficiently fixated in order to avoid electrode migration back out of the cochlea after insertion, which would again create deviations from the preoperatively planned electrode location. At the Hannover Medical Center, this fixation is accomplished by pushing the electrode lead into a slit at the facial recess after array insertion (see e.g.

One key feature of the present model are the implemented assumptions of how electrode arrays are situated inside the cochlea: rather than only assuming a consistent offset of the electrode array to the LW (Alexiades et al., 2015; Schurzig et al., 2018a), statistical data from the training dataset (evaluated according to (Salcher et al., 2021), Fig. 4A) were used to tune the model toward more realistic predictions. Our validation results (Fig. 7) demonstrate that this approach leads to significantly reduced prediction errors independent of how the individual patient anatomy was assessed, with prediction accuracy beyond previously proposed clinical results with alternative methods (Avallone et al., 2021). Nevertheless, the outcomes also indicate that predictions with the RS model achieve the highest accuracy with median errors even smaller than for the LW tracing method, which is especially noticeable in the apical cochlear region (Figs. S1 and S2). This further highlights the high precision of current models for individualized CI. These models are tuned to a patient specific anatomy-

based parameters within the basal turn of the cochlea which is, in contrast to the middle and apical cochlear turn, clearly distinguishable in clinical imaging data. The presented virtual volumetric model provides excellent estimates for individualized cochlear implantation and the decision on the most suitable electrode for the individual subject with spectacular outcome precision. A stand-out advantage of the present model is that it can be optimally linked to frequency mapping in the individual cochlea. This is of key relevance for subjects with preserved residual hearing, where the hearing portion of the cochlea may be avoided more precisely using the present virtual implantation. The frequency allocation estimate of the cochlear place could, however, not be validated in the present study. Registration of cochlear microphonics and summing potentials during cochlear implantation allow for monitoring the residual hearing during surgery (Adunka et al., 2006; Haumann et al., 2019; Calloway et al., 2014). The present virtual implantation model can also be linked to such intraoperative monitoring techniques, allowing to visualize in real-time where the array is located intracochlearly. Our model can hence not only be used for preoperative planning, but also to improve insertion monitoring intraoperatively. The frequency allocation has the additional potential of combining our model with models of current distribution in the cochlea in the future. That may more precisely predict actual electrical stimulation outcomes, and also provides a guideline for individualized speech processor programming. Therefore, we consider it a building block of future developments beyond surgical planning.

A particular strength of the present study is the large sample of subjects used for outcome validation. This was made possible by essentially including all subjects that underwent cochlear implantation at our center. We used the difference between prediction and actual position in each subject as the primary outcome measure. Including more distant measures like speech perception after implantation would not only require additional 1–3 years of collecting the data after the plateau of speech perception was achieved in each subject, it would also require the elimination of other participating factors like mother language, age at implantation, residual hearing on the same and the other ear developmental hearing loss and many more. Potential exclusion criteria would substantially diminish the group of subjects for validation and thus substantially reduce sensitivity and further involve a control group that was not using this tool. Since the primary goal was the prediction of anatomical position of the implant, and since the surgeon's applicability of the technique solely depends on the prediction precision (and not speech perception), we intentionally did not analyze other distal outcome measures in these subjects.

Another viable approach has been suggested recently: 3D printing and cochlear implantation on the printed model of the individual cochlea (Lei et al., 2021). The present approach is faster, cheaper and does neither require the surgeon's time nor does not depend on the specifics of the material used to model the cochlea and the overall size of the model. However, it requires the information of the mean distance of the given electrode from the modiolus. This may be more exact, but in prototype testing will require physical models as those suggested previously (Lei et al., 2021). Consequently, the two methods complement each other: the 3D printing approach can be optimally used in prototype electrode development, and the present approach for surgical planning after the data on the location of the implant has been collected for the given electrode.

The present virtual implantation approach was based on five different electrode designs of the same manufacturer. The model allows for the incorporation of other individualized distance data between intracochlear structures and electrode array due to the comprehensive, three-dimensional volumetric representation of the individualized cochlea. Since the prediction error was only mildly

affected by the electrode design in the present study (beyond the relation of error increasing with increasing implantation angle), we expect that the model will be similarly accurate for other electrodes. However, this remains to be tested in the future. Before these data are available (for which the method used here on 171 subjects requires replication), a constant distance may serve as a first estimate, keeping in mind the lower precision.

Here we used radial distance information of cochlear implant and LW from several surgeons. It remains to be tested whether the locational information in fact depends on the surgeon. Previously, cochlear trauma in the first turn has been documented to depend on exact implantation angle (Avci et al., 2017). This, however, concerns mostly the first half turn of the cochlea. After the implant has been inserted into the first turn, it will likely follow the shape of the cochlea and therefore the individual position will be more likely the consequence of the cochlear shape than the surgeon's exact approach.

The present model is based on high-resolution data from μ CTs and previous studies that used corrosion casts. More detailed information can be extracted from synchrotron data (Elfarnawany et al., 2017). Particularly, the frequency allocation requires the reliance on the individual assessment of the helicotrema (Helpard et al., 2021) and the hook portion (Li et al., 2007). These are very difficult to assess in μ CTs and corrosion casts, therefore the information on individual variations of these has so far relied on the few cochleae that underwent synchrotron imaging. Further increasing the number of temporal bones investigated will help to further increase the precision of the predictions.

Another limitation is the use of the mean transactional profile of the scalae for the modeling, combined with the LW. A previous study has demonstrated that the modiolar wall variability shares ~50% of the variability with the LW (Pietsch et al., 2022). In the present model modiolar variability prediction will include only this common variability since it rests on the LW spiral and a mean cross-sectional scalar profile. Particularly with respect to the modiolar hugging electrodes, an alternative model would use the tracing of the modiolar wall and add the mean profile to that, or will alternatively use both models and combine it with the cross-sectional mean profiles. There is, however, one pragmatic point to be considered: while LW tracing is possible with good precision in clinical CTs, it is not possible with the porous modiolar wall. Therefore, such models must rely more on the computer models than on tracing.

In principle, LW tracing as used in the present study requires an experienced specialist that can align the cochlea into a standardized position and determine the LW boundary reproducibly. We therefore assume that out of pragmatic reasons the models will be more frequently used than LW tracing. Automatic rendering of the LW spiral from clinical imaging may be another future step in improving the practical aspects of the method.

5. Conclusion

The present study describes an approach which allows for virtual implantations of individual patient cochleae. The model was developed and trained based on 15 μ CTs of the human cochlea as well as 171 clinical CBCT datasets of actual CI patients. Validation was performed based on additional 141 independent CBCT datasets and showed a level of accuracy which exceeds all previously proposed methods. The model does not only describe the 3D shape of the individual cochlear LW and the location of the implanted array, but also provides 3D reconstructed estimates of the intracochlear anatomy and the inserted array. The methodology therefore presents a major step toward individualized CI therapy and its application in the clinical practice.

Data availability

Data will be made available on request.

CRedit authorship contribution statement

Daniel Schurzig: Conceptualization, Methodology, Validation, Formal analysis, Investigation, Writing – original draft, Project administration, Funding acquisition. **Felix Repp:** Formal analysis, Investigation, Writing – review & editing. **Max E. Timm:** Formal analysis, Investigation, Writing – review & editing. **Cornelia Batsoulis:** Conceptualization, Supervision, Writing – review & editing. **Thomas Lenarz:** Conceptualization, Writing – review & editing, Supervision, Funding acquisition. **Andrej Kral:** Conceptualization, Formal analysis, Validation, Writing – original draft, Supervision, Funding acquisition.

Acknowledgements

The study was supported by Deutsche Forschungsgemeinschaft (DFG Exc 2177) and the MED-EL Company.

Supplementary materials

Supplementary material associated with this article can be found, in the online version, at doi:10.1016/j.heares.2022.108687.

References

- Adunka, O., et al., 2006. Monitoring of cochlear function during cochlear implantation. *Laryngoscope* 116 (6), 1017–1020.
- Alexiades, G., Dhanasingh, A., Jolly, C., 2015. Method to estimate the complete and two-turn cochlear duct length. *Otol. Neurotol.* 36 (5), 904–907.
- Anschuetz, L., et al., 2018. Cochlear implant insertion depth prediction: a temporal bone accuracy study. *Otol. Neurotol.* 39 (10), e996–e1001.
- Avallone, E., Timm, M.E., Lenarz, T., 2021. On the accuracy of insertion angle predictions with a surgical planning platform for cochlear implantation. *Otol. Neurotol.* 42 (9), e1242–e1249.
- Avci, E., Nauwelaers, T., Hamacher, V., Kral, A., 2017. Three-dimensional force profile during cochlear implantation depends on individual geometry and insertion trauma. *Ear Hear* 38 (3), e168–e179.
- Avci, E., et al., 2014. Variations in microanatomy of the human cochlea. *J. Comp. Neurol.* 522 (14), 3245–3261.
- Biedron, S., Prescher, A., Ilgner, J., Westhofen, M., 2010. The internal dimensions of the cochlear scalae with special reference to cochlear electrode insertion trauma. *Otol. Neurotol.* 31 (5), 731–737.
- Blamey, P., et al., 2013. Factors affecting auditory performance of postlinguistically deaf adults using cochlear implants: an update with 2251 patients. *Audiol. Neurotol.* 18 (1), 36–47.
- Buechner, A., Ilg, A., Majdani, O., Lenarz, T., 2017. Investigation of the effect of cochlear implant electrode length on speech comprehension in quiet and noise compared with the results with users of electro-acoustic-stimulation, a retrospective analysis. *PLoS One* 12 (5), e0174900.
- Calloway, N.H., et al., 2014. Intracochlear electrocochleography during cochlear implantation. *Otol. Neurotol.* 35 (8), 1451–1457.
- Canfarotta, M.W., et al., 2019. Validating a new tablet-based tool in the determination of cochlear implant angular insertion depth. *Otol. Neurotol.* 40 (8), 1006–1010.
- Carlson, M.L., 2020. Cochlear implantation in adults. *N. Engl. J. Med.* 382 (16), 1531–1542.
- Clark, G., 2003. *Cochlear Implants: Fundamentals and Applications*. Springer Verlag, New York.
- Dhanasingh, A., Jolly, C., 2017. An overview of cochlear implant electrode array designs. *Hear. Res.* 356, 93–103.
- Elfarnawany, M., et al., 2017. Micro-CT versus synchrotron radiation phase contrast imaging of human cochlea. *J. Microsc.* 265 (3), 349–357.
- Erixon, E., Hogstorp, H., Wadin, K., Rask-Andersen, H., 2009. Variational anatomy of the human cochlea: implications for cochlear implantation. *Otol. Neurotol.* 30 (1), 14–22.
- Erixon, E., Rask-Andersen, H., 2013. How to predict cochlear length before cochlear implantation surgery. *Acta Otolaryngol.* 133 (12), 1258–1265.
- Fedorov, A., et al., 2012. 3D Slicer as an image computing platform for the Quantitative Imaging Network. *Magn. Reson. Imaging* 30 (9), 1323–1341 11.
- Greenwood, D.D., 1990. A cochlear frequency-position function for several species - 29 years later. *J. Acoust. Soc. Am.* 87 (6), 2592–2605.

- Escudé, B., 2006. The size of the cochlea and predictions of insertion depth angles for cochlear implant electrodes. *Audiol Neurotol* 11 (Suppl. 1), 27–33.
- Hardy, M., 1938. The length of the organ of Corti in man. *Am. J. Anat.* 62, 291–311.
- Haumann, S., et al., 2019. Monitoring of the inner ear function during and after cochlear implant insertion using electrocochleography. *Trends Hear.* 23, 2331216519833567.
- Helpard, L., et al., 2020. Characterization of the human helicotrema: implications for cochlear duct length and frequency mapping. *J. Otolaryngol. Head Neck Surg.* 49 (1), 2.
- Helpard, L., et al., 2021. An Approach for Individualized Cochlear Frequency Mapping Determined From 3D Synchrotron Radiation Phase-Contrast Imaging. *IEEE Trans. Biomed. Eng.* 68 (12), 3602–3611.
- Imsiecke, M., et al., 2019a. Interaction between electric and acoustic stimulation influences speech perception in ipsilateral EAS users. *Ear Hear.* 41 (4), 868–882.
- Imsiecke, M., Buechner, A., Lenarz, T., Nogueira, W., 2019b. Psychoacoustic and electrophysiological electric-acoustic interaction effects in cochlear implant users with ipsilateral residual hearing. *Hear. Res.* 386, 107873.
- Kawano, A., Seldon, H.L., Clark, G.M., 1996. Computer-aided three-dimensional reconstruction in human cochlear maps: measurement of the lengths of organ of Corti, outer wall, inner wall, and Rosenthal's canal. *Ann. Otol. Rhinol. Laryngol.* 105 (9), 701–709.
- Koch, R.W., et al., 2017a. Evaluation of cochlear duct length computations using synchrotron radiation phase-contrast imaging. *Otol. Neurotol.* 38 (6), e92–e99.
- Koch, R.W., et al., 2017b. Measuring Cochlear Duct Length - a historical analysis of methods and results. *J. Otolaryngol. Head Neck Surg.* 46 (1), 19.
- Kral, A., Kronenberger, W.G., Pisoni, D.B., O'Donoghue, G.M., 2016. Neurocognitive factors in sensory restoration of early deafness: a connectome model. *Lancet Neurol.* 15 (6), 610–621.
- Kral, A., O'Donoghue, G.M., 2010. Profound deafness in childhood. *N. Engl. J. Med.* 363 (15), 1438–1450.
- Landsberger, D.M., Svrakic, M., Roland, J.T.J., Svirski, M., 2015. The relationship between insertion angles, default frequency allocations, and spiral ganglion place pitch in cochlear implants. *Ear Hear.* 36 (5), e207–e213.
- Lazard, D.S., Vincent, C., et al., 2012. Pre-, per- and postoperative factors affecting performance of postlinguistically deaf adults using cochlear implants: a new conceptual model over time. *PLoS One* 7, e48739.
- Lei, I.M., et al., 2021. 3D printed biomimetic cochleae and machine learning co-modelling provides clinical informatics for cochlear implant patients. *Nat. Commun.* 12 (1), 6260.
- Lenarz, T., Timm, M.E., Salcher, R., Buechner, A., 2019. Individual hearing preservation cochlear implantation using the concept of partial insertion. *Otol. Neurotol.* 40 (3), e326–e335.
- Lexow, G.J., et al., 2016. Visualization, measurement and modelling of the cochlea using rotating midmodiolar slice planes. *Int. J. Comput Assist Radiol Surg* 11 (10), 1855–1869.
- Li, P.M.M.C., et al., 2007. Anatomy of the round window and hook region of the cochlea with implications for cochlear implantation and other endocochlear surgical procedures. *Otol. Neurotol* 28 (5), 641–648.
- Li, H., et al., 2020. Synchrotron radiation-based reconstruction of the human spiral ganglion: implications for cochlear implantation. *Ear Hear.* 41 (1), 173–181.
- Margeta, J., et al., 2022. A Web-Based Automated Image Processing Research Platform for Cochlear Implantation-Related Studies. *J. Clin. Med.* 11, 6640.
- Meng, J., et al., 2016. Cochlear size and shape variability and implications in cochlear implantation surgery. *Otol. Neurotol.* 37 (9), 1307–1313.
- Mertens, G., et al., 2020. Prediction of the cochlear implant electrode insertion depth: clinical applicability of two analytical cochlear models. *Nat. Scientific Rep.* 10 (1), 3340.
- Moberly, A.C., Bates, C., Harris, M.S., Pisoni, D.B., 2016. The enigma of poor performance by adults with cochlear implants. *Otol. Neurotol.* 37 (10), 1522–1528.
- O'Connell, B.P., et al., 2017. Insertion depth impacts speech perception and hearing preservation for lateral wall electrodes. *Laryngoscope* 127 (10), 2352–2357.
- Pietsch, M., et al., 2017. Spiral form of the human cochlea results from spatial constraints. *Sci. Rep.* 7 (1), 7500.
- Pietsch, M., et al., 2022. Variations in microanatomy of the human modiolus require individualized cochlear implantation. *Sci. Rep.* 12 (1), 5047.
- Pisoni, D.B., Kronenberger, W.G., Harris, M.S., Moberly, A.C., 2017. Three challenges for future research on cochlear implants. *World J. Otorhinolaryngol. - Head Neck Surg.* 3 (4), 240–254.
- Rader, T., et al., 2016. Place dependent stimulation rates improve pitch perception in cochlear implantees with single-sided deafness. *Hear. Res.* 339, 94–103.
- Rask-Andersen, H., et al., 2011. Anatomy of the human cochlea - implications for cochlear implantation. *Cochlear Implants Int.* 12 (Suppl 1), 8–13.
- Rebscher, S.J., et al., 2008. Considerations for design of future cochlear implant electrode arrays: electrode array stiffness, size, and depth of insertion. *J. Rehabil. Res. Dev.* 45 (5), 731–747.
- Roy, A.T., et al., 2016. Deeper cochlear implant electrode insertion angle improves detection of musical sound quality deterioration related to bass frequency removal. *Otol. Neurotol.* 37 (2), 146–151.
- Salcher, R., et al., 2021. On the intracochlear location of straight electrode arrays after cochlear implantation: how lateral are lateral wall electrodes? *Otol. Neurotol.* 42 (2), 242–250.
- Schurzig, D., et al., 2019. The Use of Clinically Measurable Cochlear Parameters in Cochlear Implant Surgery as Indicators for Size, Shape, and Orientation of the Scala Tympani. *Ear Hear.* 42 (4), 1034–1041.
- Schurzig, D., et al., 2021a. Uncoiling the human cochlea - physical scala tympani models to study pharmacokinetics inside the inner ear. *Life* 11 (5), 373.

- Schurzig, D., et al., 2021b. A cochlear scaling model for accurate anatomy evaluation in cochlear implantation. *Hear. Res.* 403, 108166.
- Schurzig, D., Timm, M.E., Batsoulis, C., Lenarz, T., 2018a. Cochlear coverage estimation after cochlear implantation. *Otol. Neurotol.* 39 (8), e642–e650.
- Schurzig, D., et al., 2018b. A novel method for clinical cochlear duct length estimation toward patient-specific cochlear implant selection. *OTO Open* 2 (4). doi:10.1177/247397418800238, p.
- Schurzig, D., et al., 2018c. Cochlea helix and duct length identification – evaluation of different curve fitting techniques. *Cochlear Implants Int.* 19 (5), 268–283.
- Stakhovskaya, O., Sridhar, D., Bonham, B.H. & Leake, P.A., 2007. Frequency map for human cochlear spiral ganglion: implications for cochlear implants. *JARO* 8, 220–233.
- Timm, M.E., et al., 2018. Patient specific selection of lateral wall cochlear implant electrodes based on anatomical indication ranges. *PLoS One* 13 (10), e0206435.
- Verbist, B.M., et al., 2009. Anatomic considerations of cochlear morphology and its implications for insertion trauma in cochlear implant surgery. *Otol. Neurotol.* 30 (4), 471–477.
- Verbist, B.M., et al., 2010. Consensus panel on a cochlear coordinate system applicable in histologic, physiologic, and radiologic studies of the human cochlea. *Otol. Neurotol.* 31, 722–730.
- Würfel, W., Lanfermann, H., Lenarz, T., Majdani, O., 2014. Cochlear length determination using Cone Beam Computed Tomography in a clinical setting. *Hear. Res.* 316, 65–72.
- Wysocki, J., 1999. Dimensions of the human vestibular and tympanic scalae. *Hear. Res.* 135 (1–2), 39–46.